Potential Performance of Fully Superconducting Generators for Large Direct-Drive Wind Turbines

Dong Liu, *Member, IEEE*, Tiina Salmi, *Member, IEEE*, and Jiaxi Lin

***Abstract*—Fully superconducting generators (FSCGs) for wind turbine applications are usually synchronous machines. A high torque density should be obtained by increasing both the main field and the armature current loading. However, there are tendencies that the main field can be low but the armature current loading can be high, such as permanent magnet superconducting generators. Despite $J_c(B,T)$ characteristics and AC loss issues, simply using superconducting armature may not lead to a desired design result but deteriorate the performance with high armature reaction. This paper implements the vector-phasor diagram of non-salient synchronous generators for revealing the potential performance of only increasing the armature current loading. Three commonly used control strategies are compared. The results show that increasing the armature-field flux to a certain level will deteriorate the generator performance with all three control strategies. Comparatively, the voltage control for equaling EMF and voltage amplitudes provides the best overall performance: high torque production capability, high power factor, small power angle and a wide range of armature current loading. The results obtained from the vector-phasor diagrams are verified by finite element models with an FSCG design.**

***Index Terms*—Armature winding, control, fully superconducting generator, synchronous machine, wind turbine.**

I. Introduction

SUPERCONDUCTING generators are being studied about its suitability and feasibility for large direct-drive offshore wind turbine applications [1], [2], [3], [4], [5], [6], [7], [8]. High torque density is the core benefit from using superconducting wires to excite the main magnetic field and to power the three-phase armature winding. Partially superconducting generators (PSCGs) only use superconducting wires for the DC field winding [9], [10], [11]. The armature winding is still made of conventional copper conductors. Fully superconducting generators (FSCGs) use superconducting wires for both the field and armature windings as sketched in Fig. 1. PSCGs are more feasible at present since superconducting wires produce excessive and unacceptable AC losses in an AC environment. However, FSCGs can achieve a much higher torque density than PSCGs since the superconducting armature carries much higher current densities than copper ones [12], [13], [14], [15], [16], [17], [18].

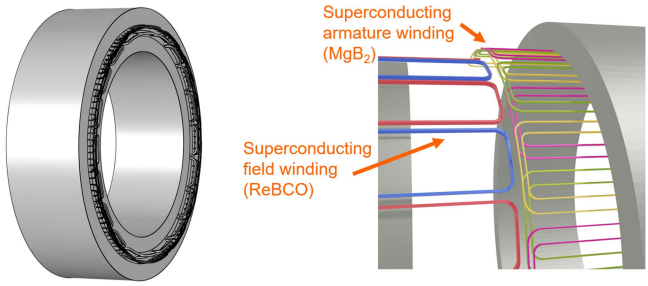

Fig. 1. 3D sketch of a fully superconducting generator with a non-salient rotor and its field and armature windings.

PSCGs and FSCGs are usually synchronous machines. The main drive for a high torque density is to increase the main field together with the armature current loading also increased. However, there are tendencies nowadays that the main field can be low but the armature current loading can be high. Such a tendency can be seen from another type of PSCGs -permanent magnet superconducting generators (PMSCGs) [19], [20], [21], [22], [23], [24], [25]. Another tendency has been seen in the studies of FSCGs where more efforts are put onto applying superconducting armature windings rather than trying to increase the main field [26], [27], [28]. The reason could be that the design work on the superconducting field windings and the partially superconducting machine topology is encountering a bottleneck regarding the torque density level and cost issues [10], [29]. These studies seem to make a detour away from the challenging superconducting field winding study. However, simply making the armature winding superconducting may not lead to a desired design result, not to mention the troublesome AC losses in superconducting AC windings. Neglecting the AC loss issue, applying superconducting armature winding should be done together with increasing the main field. Otherwise the generator performance may not reward the technical challenges and the boosted costs of superconducting AC windings.

This paper aims at finding out the performance consequences of the above-mentioned trends towards a stronger armature current loading with a weak main field. The method is to implement the vector-phasor diagram of a synchronous generator.

Manuscript received 13 November 2022; revised 27 January 2023 and 24 February 2023; accepted 1 March 2023. Date of publication 13 March 2023; date of current version 27 March 2023. This work was supported by the Academy of Finland project (HiQuench) under Grant 336287. *(Corresponding author: Dong Liu.)*

Dong Liu was with the Unit of Electrical Engineering, Tampere University, 33720 Tampere, Finland. He is now with the School of Energy Systems, LUT University, FI-15210 Lahti, Finland (e-mail: dong.liu@lut.fi).

Tiina Salmi is with the Unit of Electrical Enginerring, Tampere University, FI-33720 Tampere, Finland.

Jiaxi Lin was with the Hohai University, Nanjing CN-211100, China.

Color versions of one or more figures in this article are available at https://doi.org/10.1109/TASC.2023.3255826.

Digital Object Identifier 10.1109/TASC.2023.3255826

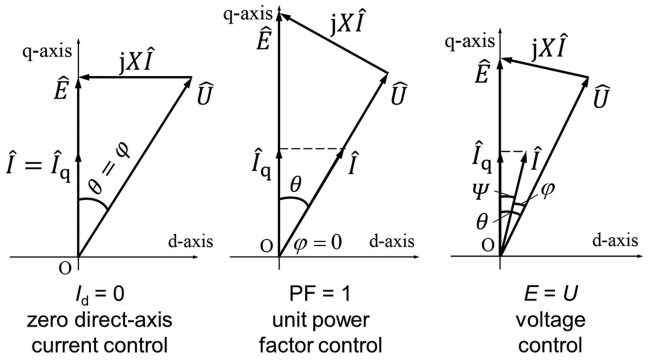

Fig. 2. Phasor diagram of three commonly used control strategies for direct-drive wind turbine generators with a non-salient rotor.

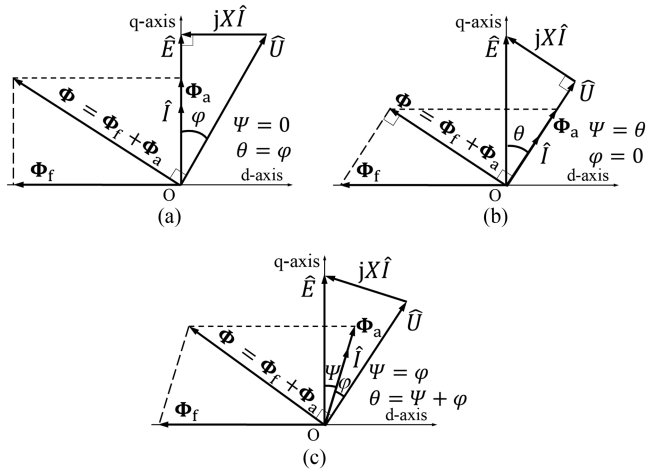

Fig. 3. Vector-phasor diagrams of the three control strategies, (a) zero direct-axis current control, (b) unit power factor control, (c) $E = U$ voltage control.

Only non-salient generators are considered in the study. Salient generators are a bit different and will be studied in future. The results of the study can also be used for generic synchronous generators with a non-salient rotor. The study method is irrelevant to winding materials and thus the $J_c(B,T)$ limitations and AC losses of superconducting wires are not considered. We believe that the potential performance revealed in the study shows the best case. The potential performance will definitely become worse when the $J_c(B,T)$ characteristics and AC losses are taken into account. Three commonly used control strategies for direct-drive wind turbine generators are investigated since they have different vector-phasor diagrams. The results obtained from the vector-phasor diagrams are verified by finite element models with a practical electromagnetic design of an FSCG.

II. Control Strategies

Within all possible control strategies for direct-drive wind turbine generators, three commonly used ones are chosen for the study. They are zero direct-axis current control ($I_d = 0$), unit power factor control (PF = 1) and voltage control ($E = U$) [30], [31]. Their phasor diagrams are illustrated in Fig. 2. Here we assume that the rotor is not salient so that the direct and quadrature axes of the generator have the same synchronous reactance X. The electromotive force (EMF) $\hat{E}$ leads the terminal voltage $\hat{U}$. In the zero direct-axis control, the current $\hat{I}$ is in phase with $\hat{E}$. In the unit power factor control, $\hat{I}$ is in phase with $\hat{U}$. In the voltage control, $\hat{I}$ is right in the middle of $\hat{E}$ and $\hat{U}$, thereby making $E = U$. The quadrature-axis component of the current $\hat{I}_q$ is the torque-producing component. The angle φ is the power factor angle which is between $\hat{U}$ and $\hat{I}$. The angle θ is the power angle between $\hat{E}$ and $\hat{U}$. The angle ψ is the internal power factor angle between $\hat{E}$ and $\hat{I}$. Their relationship is then $\theta = \psi + \varphi$. The cap notation on top means that the quantity is a phasor. Without the cap the quantity means the length of the phasor.

III. Vector-Phasor Diagrams

The three control strategies have their own vector-phasor diagram as shown in Fig. 3. A vector-diagram is based on the phasor diagram but the space vectors of magnetic fluxes are added to the phasor diagram. The space vectors and phasors are related and put together by the link of the phasor $\hat{E}$ since $\hat{E}$ is defined in phase with the quadrature axis. The EMF $\hat{E}$ is induced by the main-field flux vector $\mathbf{\Phi_f}$ which is excited by the field current. Thus, $\hat{E}$ lags $\mathbf{\Phi_f}$ by 90°. The armature-field flux vector $\mathbf{\Phi_a}$ is produced by the magnetomotive force of armature current $\hat{I}$ and they are thus in phase. The air gap flux vector $\mathbf{\Phi}$ in the resultant flux of $\mathbf{\Phi_f}$ and $\mathbf{\Phi_a}$ and induces the air gap voltage $\hat{E}_\delta$. Here we neglect the resistance of the armature winding. Then, the terminal voltage $\hat{U}$ is equal to $\hat{E}_\delta$. Since $\hat{E}_\delta$ lags $\mathbf{\Phi}$ by 90°, $\hat{U}$ also lags $\mathbf{\Phi}$ by 90°.

In the zero direct-axis control, the phasor $jX\hat{I}$ is perpendicular to $\hat{E}$ and $\mathbf{\Phi_a}$ is perpendicular to $\mathbf{\Phi_f}$. In the unit power factor control, the phasor $jX\hat{I}$ is perpendicular to $\hat{U}$ and $\mathbf{\Phi_a}$ is perpendicular to $\mathbf{\Phi}$. In the voltage control, E equals U, $\mathbf{\Phi_f}$ equals $\mathbf{\Phi}$, and ψ equals φ.

According to the relationships in the vector-phasor diagrams, we can derive the equations given below to calculate the electromagnetic torque T_e, power factor $\cos\varphi$, power angle θ, and voltage normalized to EMF (U/E) as the performance indicators. Note that (1)–(13) are independent of generator topology since they apply to all synchronous generators.

$$U/E = \frac{\Phi}{\Phi_f} \tag{1}$$

1) Zero Direct-Axis Control:

$$\Phi = \sqrt{\Phi_f^2 + \Phi_a^2} \tag{2}$$

$$\cos\varphi = \frac{\Phi_f}{\Phi} \tag{3}$$

$$T_e = K \cdot \Phi \cdot \Phi_a \cdot \sin\left(\Phi, \overset{\wedge}{\Phi}_a\right) = K \cdot \Phi \cdot \Phi_a \cdot \cos\varphi \tag{4}$$

where K is the constant for torque.

2) Unit Power Factor Control:

$$\Phi = \sqrt{\Phi_f^2 - \Phi_a^2} \tag{5}$$

$$\cos\varphi = 1 \tag{6}$$

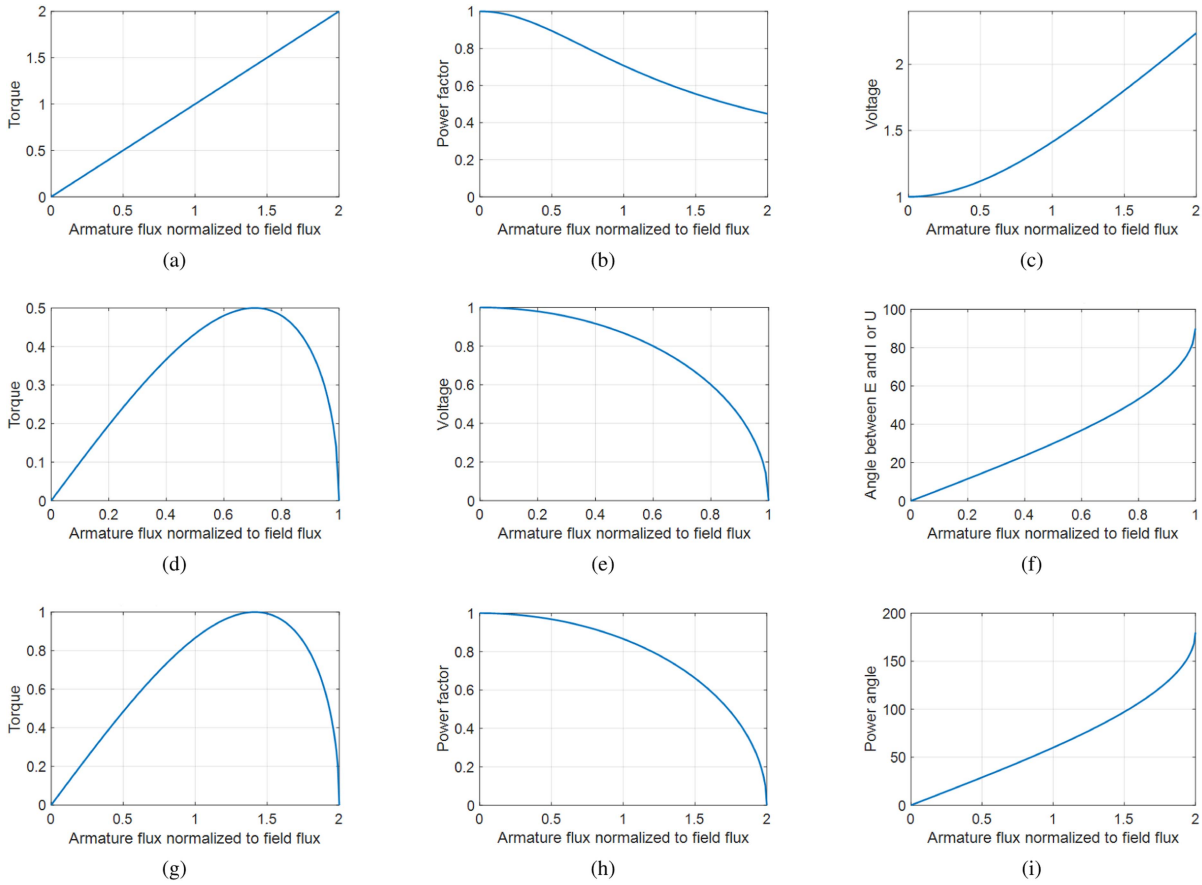

Fig. 4. Performance of the three control strategies obtained from vector-phasor diagrams, (a)–(c) zero direct-axis current control: (a) torque production, (b) power factor, (c) voltage ratio U/E; (d)–(f) unit power factor control: (d) torque production, (e) voltage ratio U/E, (f) power angle; (g)–(i) $E = U$ voltage control: (g) torque production, (h) power factor, (i) power angle.

$$\theta = \arcsin \frac{\Phi_{\mathrm{a}}}{\Phi_{\mathrm{f}}} \tag{7}$$

$$T_{\mathrm{e}} = K \cdot \Phi \cdot \Phi_{\mathrm{a}} \cdot \sin\left(\Phi, \overset{\wedge}{\Phi}_{\mathrm{a}}\right) = K \cdot \Phi \cdot \Phi_{\mathrm{a}} \cdot \sin 90^{\circ} \tag{8}$$

3) Voltage Control:

$$\Phi = \Phi_f \tag{9}$$

$$\varphi = \psi = 0.5 \cdot \arcsin\left[1 - 0.5 \cdot \left(\frac{\Phi_{\mathrm{a}}}{\Phi_{\mathrm{f}}}\right)^2\right] \tag{10}$$

$$\theta = \arcsin \frac{\Phi_{\mathrm{a}}}{\Phi_{\mathrm{f}}} \tag{11}$$

$$T_{\mathrm{e}} = K \cdot \Phi \cdot \Phi_{\mathrm{a}} \cdot \sin\left(\Phi, \overset{\wedge}{\Phi}_{\mathrm{a}}\right) = K \cdot \Phi \cdot \Phi_{\mathrm{a}} \cdot \sin\left(90^{\circ} - \varphi\right) \tag{12}$$

$$\theta = 2\varphi = 2\psi \tag{13}$$

IV. Performance

The purpose of the paper is to show the effects of armature current loading on the performance. Thus, we fix the main-field flux vector length to be $\Phi_{\mathrm{f}} = 1$ and let the armature-field flux vector length Φ_{a} range from 0 to a higher level normalized to the main-field flux vector length Φ_{f}. All the performance indicators will thus be presented in relative values. Such a fixation will show a full range of armature flux with respect to the main flux. The fixation will also show the effects of armature flux when it is increased to be comparable to the main flux or even higher, which points out the limit of armature field enhancement by superconductivity. The results of performance indicators as a function of the armature-field flux normalized to the main-field flux are shown in Fig. 4. Note that operation of direct-drive wind turbines applies the same control strategy throughout the rated and partial loads.

1) Zero Direct-Axis Control: The torque T_{e} with respect to the armature flux is shown in Fig. 4(a). As the armature flux increases, the torque will increase linearly and have no peaks or turning points. This is the advantage of using the zero direct-axis control. However, as shown in Fig. 4(b), the power factor drops fast as the armature flux increases. When the armature flux increases to a half of the field flux and the same, the power factor drops to less than 0.9 and 0.7, respectively. Such a low power factor will require a higher capacity for the power electronic converter to handle the reactive current. Another drawback of this control strategy is that the voltage is never lower than the EMF and is very easy to become much higher than the EMF as shown in Fig. 4(c). In other words, the no-load voltage

can become quite low with a great armature reaction since the generator has been rated with its full-load voltage.

2) Unit Power Factor Control: The torque is shown in Fig. 4(d) and has a peak when the armature flux is $\sqrt{2}/2$ times the field flux. The peak production of torque is however only 0.5 K. A higher armature flux will then lead to a lower torque. The torque drops to zero when the armature flux is equal to the main flux. This means that the unit power factor control has the weakest torque capability among the three control strategies. The benefit is that the power electronic converter does not have to supply extra reactive power. Another drawback is the voltage drops rapidly as the armature flux increases (Fig. 4(e)). When the armature flux equals the main flux, the voltage will become vanished. In other words, an EMF which is much higher than the rated voltage is needed to make the terminal voltage as high as rated if the armature flux is designed to be high. The extreme case is when the armature flux equal the main flux. Then the EMF will go infinitely high. The power angle, as shown in Fig. 4(f), cannot exceed but approach 90°. All these three results indicate that generator performance will be deteriorated as the armature flux goes beyond a certain level (e.g., $\sqrt{2}/2$ times the main flux). The most critical problem is the poor torque production capability which is opposing the purpose of using superconducting armature windings.

3) Voltage Control: Like the unit power factor control, as shown in Fig. 4(g), the torque also has a peak. However, the differences are that the peak occurs when the armature flux is $\sqrt{2}$ times the field flux and the peak torque is as high as 1.0 K. The torque capability is doubled. The torque will be vanished when the armature flux is as high as twice the main flux, but the armature field usually does not need at all to reach such a high level. The power factor, as shown in Fig. 4(h), is also reduced with a higher armature flux but the drop is mild. The power factor will stay higher than 0.85 even when the armature flux equals the main flux. As shown in Fig. 4(i), the power angle will reach 90° when the armature flux is about $\sqrt{2}$ times the main flux. The large power angle over 90° will not cause stability issues to the generator, since the back-to-back converter of the generator can keep the power angle below 90°. Then, the maximum torque production just occurs at 90°. This control strategy does not have the issues with the other two control strategies. It also makes full use of the insulation rating since the voltages at no load and full load are equal. Hence, the voltage control has the best overall performance.

V. Verification by Finite Element Methods

The results obtained from the calculations with the vector-phasor diagrams are verified with a finite element (FE) model. The model is based on a 20 MW FSCG concept from [17] but the field winding is made of ReBCO tapes instead of MgB_2 wires. The design will be seen in [32]. The design aims at low weight, less iron, non-salient rotor and slotless stator but magnetic isolation. The rotor and stator both have back iron. There is no iron in the rotor poles and stator teeth. Iron saturation and resulting saliency between the d- and q-axis are included in the model using B-H curves. The distance between the armature winding and the field winding accommodates two individual cryostats for the rotor and stator. The line-to-line EMF is kept 6.6 kV. Keeping the same field excitation by the field winding, the armature current loading is increased to simulate the armature-field flux range as used in Fig. 4.

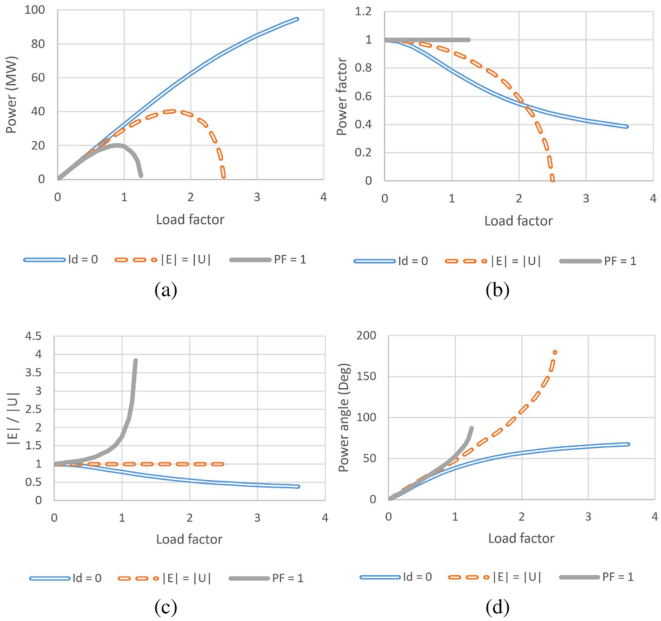

Fig. 5. Performance comparison obtained from the finite element model of an FSCG design obtained from vector-phasor diagrams, (a) power, (b) power factor, (c) E/U, (d) power angle.

The model is built and computed with COMSOL Multiphysics. The results are shown in Fig. 5, indicating the trends of power $P = T_e\omega_m$, power factor, E/U and power angle θ with respect to the load factor, where ω_m is the rated mechanical angular frequency of the rotor. The load factor is the linear current density normalized to its rated value. The curves extend to an identifiable level where we can evaluate which control strategy has a higher potential of increasing armature current loading. The trends agree with the results from Section IV. Again, we can clearly see the difference of power or torque production capability among the three control strategies in Fig. 5(a). We also see the direct comparison of power factor drops in Fig. 5(b) and the challenges of voltage variation in Fig. 5(c).

VI. Conclusion

Better use of the high current density capability of superconductors in the armature winding results in a high armature-produced magnetic field. We used vector-phasor diagrams of non-salient synchronous generators to calculate the potential performance of FSCGs without saliency when the armature-field flux becomes higher. These calculations were verified by an FE model of an FSCG design modified from the literature.

Three most used control strategies were analyzed for how the increased armature field influences the performance and where the limit of the performance is. From the results of electromagnetic torque, power factor, voltage and power angle, we see that the armature field cannot be unlimitedly increased. Otherwise,

the performance will be deteriorated even if $J_c(B,T)$ characteristics and AC losses are still neglected.

The zero direct-axis current control has no upper limits of torque and thus has the highest potential of torque production. With higher armature fields, however, its power factor becomes quite low (e.g., 0.7 with the armature field equaling the main field) and voltage variation from no load to full load is significant. The unit power factor control leads to the poorest overall performance. The voltage control for $E = U$ provides the best overall performance: a high torque, high power factor, small power angle and wide range of armature current loading. However, the zero direct-axis current can compete with the voltage control if a low power factor does not matter.

The results of the study assumed a fixed main-field flux. The main field excitation has to be boosted as well if an even higher torque production is needed compared to the predicted in the study. Combination of a strong main field and a reasonably high armature field (e.g., much lower than the main field) is thought to provide the best overall performance: high torque, high power factor, small voltage variation with load, and foreseen lower AC losses. The potential performance of FSCGs as a result of the combination will be studied with $J_c(B,T)$ and AC losses in the future.

REFERENCES

[1] K. S. Haran et al., "High power density superconducting rotating machines–Development status and technology roadmap," *Supercond. Sci. Technol.*, vol. 30, 2017, Art. no. 123002.

[2] B. B. Jensen, N. Mijatovic, and A. B. Abrahamsen, "Development of superconducting wind turbine generators," *J. Renewable Sustain. Energy*, vol. 5, 2013, Art. no. 023137.

[3] H. Polinder, J. A. Ferreira, B. B. Jensen, A. B. Abrahamsen, K. Atallah, and R. A. McMahon, "Trends in wind turbine generator systems," *IEEE J. Emerg. Sel. Topics Power Electron.*, vol. 1, no. 3, pp. 174–185, Sep. 2013.

[4] I. Marino et al., "Lightweight MgB_2 superconducting 10 MW wind generator," *Supercond. Sci. Technol.*, vol. 29, Feb. 2016, Art. no. 024005.

[5] X. Song et al., "Designing and basic experimental validation of the world's first MW-class direct-drive superconducting wind turbine generator," *IEEE Trans. Energy Convers.*, vol. 34, no. 4, pp. 2218–2225, Dec. 2019.

[6] X. Song et al., "Commissioning of the world's first full-scale MW-class superconducting generator on a direct drive wind turbine," *IEEE Trans. Energy Convers.*, vol. 35, no. 3, pp. 1697–1704, Sep. 2020.

[7] X. Song et al., "Ground testing of the world's first MW-class direct-drive superconducting wind turbine generator," *IEEE Trans. Energy Convers.*, vol. 35, no. 2, pp. 757–764, Jun. 2020.

[8] X. Song et al., "Experimental validation of a full-size pole pair set-up of an MW-class direct drive superconducting wind turbine generator," *IEEE Trans. Energy Convers.*, vol. 35, no. 2, pp. 1120–1128, Jun. 2020.

[9] R. Qu, Y. Liu, and J. Wang, "Review of superconducting generator topologies for direct-drive wind turbines," *IEEE Trans. Appl. Supercond.*, vol. 23, no. 3, Jun. 2013, Art. no. 5201108.

[10] D. Liu, H. Polinder, A. B. Abrahamsen, and J. A. Ferreira, "Topology comparison of superconducting generators for 10-MW direct-drive wind turbines: Cost of energy based," *IEEE Trans. Appl. Supercond.*, vol. 27, no. 4, Jun. 2017, Art. no. 5202007.

[11] R. Fair et al., "Superconductivity for large scale wind turbines," U.S. Department of Energy Tech. Rep. DE-EE0005143, Apr. 2012.

[12] T. Balachandran, D. Lee, N. Salk, J. Xiao, and K. S. Haran, "Evaluation and mitigation of AC losses in a fully superconducting machine for wind turbine applications," *IEEE Trans. Appl. Supercond.*, vol. 30, no. 4, Jun. 2020, Art. no. 5207005.

[13] T. Balachandran, D. Lee, N. Salk, and K. S. Haran, "A fully superconducting air-core machine for aircraft propulsion," *IOP Conf. Ser.: Mater. Sci. Eng.*, vol. 756, Jul. 2019, Art. no. 012030.

[14] D. Lee, T. Balachandran, H.-W. Cho, and K. Haran, "Exploring fully superconducting air-core machine topology for off-shore wind turbine applications," *IEEE Trans. Magn.*, vol. 55, no. 7, Jul. 2019, Art. no. 8106506.

[15] C. D. Manolopoulos et al., "Comparison between coreless and yokeless stator designs in fully-superconducting propulsion motors," *IEEE Trans. Appl. Supercond.*, vol. 30, no. 6, Sep. 2020, Art. no. 5207407.

[16] S. S. Kalsi, "Superconducting wnd turbine generator employing MgB_2 windings both on rotor and stator," *IEEE Trans. Appl. Supercond.*, vol. 24, no. 1, Feb. 2014, Art. no. 5201907.

[17] T. Hoang, L. Quéval, C. Berriaud, and L. Vido, "Design of a 20-MW fully superconducting wind turbine generator to minimize the levelized cost of energy," *IEEE Trans. Appl. Supercond.*, vol. 28, no. 1, Jun. 2018, Art. no. 5206705.

[18] P. Masson et al., "Development of a 3D sizing model for all-superconducting machines for turbo-electric aircraft propulsion," *IEEE Trans. Appl. Supercond.*, vol. 23, no. 3, Jan. 2013, Art. no. 3600806.

[19] K. Zhang, X. Huang, L. Wu, Y. Fang, and W. Cao, "Stator design aspects for permanent magnet superconducting wind power generators," *IEEE Trans. Appl. Supercond.*, vol. 29, no. 2, Mar. 2019, Art. no. 5201205.

[20] X. Huang, K. Zhang, L. Wu, Y. Fang, and Q. Lu, "Design of a dual-stator superconducting permanent magnet wind power generator with different rotor configuration," *IEEE Trans. Magn.*, vol. 53, no. 6, Jun. 2017, Art. no. 8700204.

[21] X. Huang, C. Zhou, K. Zhang, L. Wu, J. Zhang, and W. Cao, "Comparison of electromagnetic performance of SCPM wind power generators with different topologies," *IEEE Trans. Appl. Supercond.*, vol. 29, no. 2, Mar. 2019, Art. no. 5201405.

[22] P. Song et al., "Development and testing of a 2.5 kW synchronous generator with a high temperature superconducting stator and permanent magnet rotor," *Supercond. Sci. Technol.*, vol. 27, 2014, Art. no. 044026.

[23] D. Liu et al., "Short-circuit characteristics of superconducting permanent magnet generators for 10 MW Wind turbines," *IEEE Trans. Appl. Supercond.*, vol. 31, no. 5, Aug. 2021, Art. no. 5201005.

[24] S. Xue et al., "Stator optimization of wind power generators with high-temperature superconducting armature windings and permanent magnet rotor," *IEEE Trans. Appl. Supercond.*, vol. 31, no. 2, Mar. 2021, Art. no. 5200410.

[25] X. Li, K. Lu, Y. Zhao, D. Chen, P. Yi, and W. Hua, "Incorporating harmonic-analysis-based loss minimization into MPTC for efficiency improvement of FCFMPM motor," *IEEE Trans. Ind. Electron.*, vol. 70, no. 7, pp. 6540–6550, Jul. 2022.

[26] D. Liu, U. Hasanov, C. Ye, X. Gou, and X. Wang, "Design considerations and short-circuit characteristics of fully superconducting wind turbine generators," in *Proc. IEEE 12th PES Asia-Pacific Power Energy Eng. Conf.*, 2020, pp. 1–6.

[27] A. Kawagoe et al., "Numerical analyses on the influences of armature winding shape and yoke arrangements on total losses in fully superconducting synchronous motors using REBCO tapes," *IEEE Trans. Appl. Supercond.*, vol. 28, no. 4, Jun. 2018, Art. no. 5208104.

[28] P. Song et al., "Thermal analysis for the HTS stator consisting of HTS armature windings and an iron core for a 2.5 kW HTS generator," *Supercond. Sci. Technol.*, vol. 29, 2016, Art. no. 054007.

[29] D. Liu, H. Polinder, A. B. Abrahamsen, and J. A. Ferreira, "Potential of partially superconducting generators for large direct-drive wind turbines," *IEEE Trans. Appl. Supercond.*, vol. 27, no. 5, Aug. 2017, Art. no. 5203711.

[30] B. Wu, Y. Lang, N. Zargari, and S. Kouro, "Variable-speed wind energy systems with synchronous generators," in *Power Conversion and Control of Wind Energy Systems*. Hoboken, NJ, USA: Wiley, 2011, pp. 275–316.

[31] H. Polinder, F. F. A. van der Pijl, G. de Vilder, and P. J. Tavner, "Comparison of direct-drive and geared generator concepts for wind turbines," *IEEE Trans Energy Convers.*, vol. 21, no. 3, pp. 725–733, Sep. 2006.

[32] J. Lin, D. Liu, and Y. Wu, "Concentric-coil distributed winding design for large direct-drive fully superconducting machines," *IEEE Trans. Appl. Supercond.*, vol. 33, no. 5, Aug. 2023, Art. no. 5201005.